

# IR Spectrometer Project for the BTA Telescope

V. L. Afanasiev, E. V. Emelianov, and V. A. Murzin  
*Special Astrophysical Observatory, Russian Academy of Sciences, Nizhnii Arkhyz, 369167 Russia*

V. F. Vdovin  
*Institute of Applied Physics, Russian Academy of Sciences, Nizhny Novgorod, 603950 Russia and  
 Nizhny Novgorod State Technical University, Nizhny Novgorod, 603950 Russia*

## 1. INTRODUCTION

The aim of the project is to extend the wavelength range accessible for observations on the 6-m BTA telescope toward near infrared ( $0.8 \div 2.5 \mu\text{m}$ ). This wavelength interval is productive for the study of “cool” objects ( $T < 2000 \text{ K}$ ), dust enshrouded sources, and objects with redshifts up to  $z = 10$ . The near infrared range contains lines that are of interest for spectral diagnostics: rotational-vibrational bands of molecules important in astrophysics (such as CO, OH, SiO, CH, CN, NH, H<sub>2</sub>O, HCN, CH<sub>4</sub>, etc.), rotational transitions of H<sub>2</sub>, numerous transitions of neutral and ionized atoms. The list of astrophysical tasks addressable with the 6-m BTA telescope in the near IR is rather extensive and may include such studies as:

- spectroscopy of protoplanetary nebulae;
- search for exoplanets and brown dwarfs;
- spectroscopy and photometry of regions of violent star formation in our Galaxy and in the nearby and distant ( $z < 10$ ) galaxies;
- stellar kinematics and morphology of systems of various stellar populations in spiral galaxies;
- physical conditions in ionized gas, stellar kinematics and morphology in active galactic nuclei (AGN) and starburst galaxies;
- ultraluminous infrared galaxies (ULIRG);
- determination of photometric redshifts from the spectral energy distribution (SED).

### 1.1. Specificities of the Design of IR Facilities

#### 1.1.1. Photometry

The Earth’s atmosphere affects appreciably the IR radiation that passes through it. Atmospheric absorption and scattering of IR radiation is quite significant and, moreover, has an irregular nature, determined by the spectral features of the absorption of IR waves by the principal atmospheric gaseous components, and first and foremost by water. Therefore photometric observations

in the IR are performed mainly in atmospheric “transparency windows”. The transmission maxima of the I, J, H, and K-band filters coincide with those of the Earth’s atmosphere.

The so-called cold pupil stop is usually employed in IR photometers to reduce thermal blackbody noise from the telescope structures: a cooled diaphragm is placed in the exit pupil plane to block such noise sources as the primary focus cabin and the mirror holder. All the other optical parts of the photometer may be warmer, because their contribution to the total noise is less important.

Cooling the exit pupil is impossible without extra optics, and therefore when the instrument is operated in the photometric mode a focal reducer has to be incorporated into the optical scheme even if the aperture ratio is unchanged. To match the telescope scale with the pixel size, it is better to reduce the image scale at the detector, i.e., increase the aperture ratio.

As an example of an IR photometer in actual operation, let us consider FourStar, a photometer with a large field of view developed for the 6.5-m Magellan Baade telescope of the Las Campanas observatory [1]. The instrument has a  $10.9 \times 10.9$  field of view. Its detector consists of a  $2 \times 2$  array of HAWAII-2RG. The collimator of the instrument also serves as the entrance window. The image of the exit pupil produced by the collimator is located immediately in front of the camera. The main sources of thermal noise are shielded by a cooled mask. The optical parts of the camera are cooled to 200 K. The filters, field correction lenses, and detector located in the converging beam after the camera are cooled to 77 K. The filters are placed on two six-slot filter wheels. The cryostat of the instrument has the form a cylindrical structure with a diameter and length of 0.9 and 3 m, respectively. About 45 l of liquid nitrogen are needed to maintain the operating temperature for 24 hours.

In 2005 the Special Astrophysical Observatory acquired a CIRSI camera with two hybrid HAWAII-1 HgCdTe detectors to perform near-infrared photometry at the 6-m BTA telescope. These detectors operate in the  $0.8 \div 2.5 \mu\text{m}$  wavelength range [2].

The dewar with the camera, computer, and controller are located on a  $0.9 \times 0.9 \times 0.75 \text{ m}^3$  frame [3]. When assembled, the entire structure has a mass of about 200 kg. It can therefore be mounted only on rather large telescopes. One detector covers a  $2.9 \times 2.9$  sky area when operating in the primary focus of the 6-m BTA telescope without a focal reducer.

Numerous attempts to get CIRSI into working condition have failed: cryostat leaks could not be eliminated even to a degree that would allow laboratory tests to be performed. CIRSI electronics have become aged and obsolete: they were developed in 1997 [4] and cannot interoperate with modern data acquisition and reduction systems.

In our opinion, the most rational way to revive the available IR equipment is to develop new hardware, where the only parts left from CIRSI would be the detectors.

### 1.1.2. Spectroscopy

IR spectroscopy is a relatively new trend in observational astronomy, which has a great research potential. Interstellar extinction decreases rapidly toward longer wavelengths and therefore infrared observations may provide data on objects that are hidden by optically thick dust and gas layers when observed in the visible range. Furthermore, galaxies at large  $z$  can be studied only in the IR because the main spectral line features are redshifted.

The IR spectrographs currently used on major telescopes suffer from many impassable limitations. Among them is the small width of the spectral interval covered by a single exposure. In addition, high-resolution IR spectrographs are very expensive and highly specialized instruments. Relaxing the diffraction-limited resolution requirement would make it possible to extend the application domain of the instrument and make it more universal.

IR spectrographs actually differ little from their visual counterparts except that they require deeper cooling of the parts. Many published technical solutions can be found for such spectrographs, however, they are all essentially confined to focal reducers with a grating or prism placed in the exit pupil to serve as a dispersive element. Such a spectrograph is evidently easy to convert into a photometer.

Mixed-mode instruments can operate in two modes: as a photometer and as a spectrometer. For example, for the Nasmyth focus of the 10-m Subaru telescope a cooled IR-range camera/spectrograph CISCO was developed [5]. The entire instrument is housed in a cylindrical cryostat, where the pressure and temperature are maintained at about  $10^{-5}$  Pa and  $54 \div 59$  K, respectively. The instrument (when operating in the spectrograph mode) has a spectral resolution of about  $200 \div 250$  in the  $0.8 \div 2.5 \mu\text{m}$  wavelength interval. The operation mode of the instrument can be changed by replacing the elements (the prism, set of grisms, and filter kit) installed on the stepper motor controlled wheel. The readout noise and dark current are sufficiently low to allow the instrument to be used for faint objects ( $22.^m4$  and  $19.^m7$  photometric and and forspectroscopic observations, respectively).

The 1.88-m telescope of the Japanese Okayama ob-

servatory is equipped with the IR camera/spectrograph OASIS, used both for photometry and long-slit spectroscopy [6]. The instrument employs  $256 \times 256$  px HgCdTe NICMOS-3 arrays. In the case of photometric observations the resolution is  $0.^{\prime\prime}97/\text{pixel}$ , and when operated in the long-slit spectroscopy mode the instrument provides a spectral resolution  $R = 150 \div 1000$  (depending on the chosen grating: 300 or 75 lines/mm). The optical parts of the instrument are cooled to 110 K, whereas the detector temperature is maintained at 80 K (cooling the instrument from room to operating temperature takes about two days).

### 1.1.3. Detectors

The operation of most of the near- and mid-infrared detectors is based on the photoelectric effect. Charges arising as a result of the internal photoelectric effect can be accumulated in potential wells like in a CCD cell, or the photo-conduction current created by these charges can be recorded and amplified immediately. Detectors can also be based on external photoelectric effect.

Currently, two-dimensional IR detectors are mostly based on HgCdTe chips manufactured using various technologies. Let us list their main differences from CCDs [7].

- Each pixel combines not only a cell to accumulate the electrons emitted as a result of the internal photoelectric effect, but also an amplifier. The by-effect is that the detector gain varies from pixel to pixel.
- In the readout process, the charge accumulated by a CCD cell must pass through several other such cells, whereas the signal from a single pixel of a HgCdTe chip is read directly (via multiplexing of outputs). Hence there is no charge transfer noise in detectors of this type, resulting in reduced readout noise.
- The CMOS multiplexer allows the signal to be read off the cells of the HgCdTe array in arbitrary order, which is beyond the capabilities of CCDs.
- Another advantage of detectors based on CMOS multiplexers is that they allow nondestructive signal readout: the current state of the charge accumulated by array cells can be read out at any time during exposure without fatal distortion.

Since the free charge carriers form in the semiconductor not only when induced by photons, but also due to thermal energy, the detector has to be cooled to reduce noise. The operating temperature of the detector decreases with increasing wavelength. The operating temperature limit of the detector can be approximately computed by the formula  $T_{max} = \frac{200}{\lambda_{max}}$ , where temperature is in Kelvin and the long-wavelength cut-off is in microns.

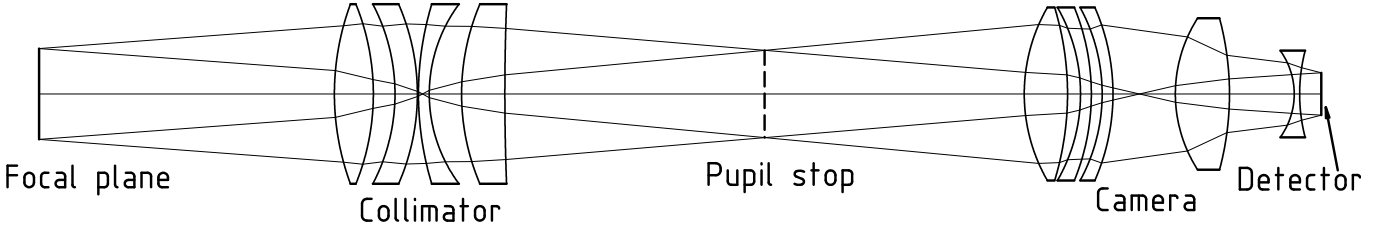


Figure 1: Optical scheme of the IR focal reducer.

Given that all the properties of the CMOS multiplexer are sensitive to its operating temperature, the optimum temperature should be chosen carefully for each detector and maintained with high stability throughout the entire exposure.

The  $1024 \times 1024$  px HAWAII-1 HgCdTe detector array (with a pixel size of  $18.5 \times 18.5 \mu\text{m}$ ) acquired by the Special Astrophysical Observatory has its maximum quantum efficiency (60% at  $T = 78\text{ K}$ ) in the  $1.9 \div 2.5 \mu\text{m}$  wavelength interval. The depth of the potential well of the detector cells is  $100\text{ Ke}^-$ . The gain in the original readout system is about  $8\text{ e}^-/\text{ADU}$ . The detector response curve is linear to within 1% in the  $3000 \div 7000$  ADU interval [8].

HAWAII arrays are combined instruments with an individual preamplifier for each element, resulting in a highly increased pixel-by-pixel nonuniformity of the detector. This creates additional challenges at the stage of reduction of the acquired data. Special image reduction techniques (correlated double sampling at readout, post-readout reduction of the array of intermediate images) can be used to increase the dynamic range of the detector.

#### 1.1.4. Optical Components

Given that most of the materials used in visual optics are to a certain degree opaque for infrared radiation, new IR materials have to be studied and implemented. High-resistivity silicon is the classical material used in the infrared: it is a replacement of sorts for glass that is employed in the visible range. Also used in the IR is chalcogenide glass (various metal compounds with elements of the sixth periodic group—oxygen, sulphur, selenium, tellurium, and polonium). Most of these compounds are transparent for radiation with wavelengths up to  $11 \div 12 \mu\text{m}$ . Composite glasses allow this wavelength range to be further expanded to  $18 \div 20 \mu\text{m}$ .

IR filters are often made using the same techniques as those employed for the visible range. For example, absorption cells or multiple reflection filters may be used as broadband filters. Fabry-Perot etalons can be used to filter narrow IR bands. Broader photometric bands can be created with interference filters.

The rather large width of the near IR spectral range ( $0.8 \div 2.5 \mu\text{m}$ ) combined with the resolution of  $R = 1000 \div 3000$  prevents making an efficient spectrograph with a single diffraction grating. However, the use of a set of changeable gratings complicates the design and increases the size of the cryostat, ultimately raising the cost of the entire instrument. Furthermore, classical “ruled” gratings are a bad choice for the infrared, because (1) their efficiency decreases sharply with decreasing grating period (thereby reducing the limiting resolution of the instrument) and (2) the grating itself becomes very unwieldy (otherwise the diffraction efficiency of the instrument would decrease even further because of the too wide instrumental function).

Volume Phase Holographic Gratings (VPHG) [9] have been used extensively in astronomical observations in recent years. Unlike classical gratings, which use spatial modulation, VPHG also uses modulation of the refraction index within a thin layer of dichromated gelatin of which the VPHG is made. The gelatin layer must be thicker than the maximum wavelength of the considered spectral interval.

The physics of light diffraction on VPHG is similar to the mechanism of X-ray scattering on crystal lattices. VPHG reach maximum efficiency if the Bragg conditions are satisfied, which is equivalent to mirror reflection from planes of constant refraction index. The base wavelength satisfying the Bragg condition can be changed by varying the angle of light incidence onto the grating. Hence the maximum diffraction efficiency can be achieved over a sufficiently wide wavelength interval by changing the Bragg angle. The maximum quantum efficiency of a VPHG may be as high as 90  $\div$  95% even if the radiation wavelength is comparable to the grating period (the efficiency of common gratings is known to decrease sharply in this case). Other advantages of VPHG include weak scattering and weak dependence of the grating efficiency on the polarization of the radiation flux studied.

## 2. OPTICAL ARRANGEMENT OF THE SPECTROMETER

The proposed optical arrangement (Fig. 1) includes a four-lens  $F/4$  collimator with a focal length of  $F = 160\text{ mm}$ , and a five-lens  $F/2$  camera with a focal length

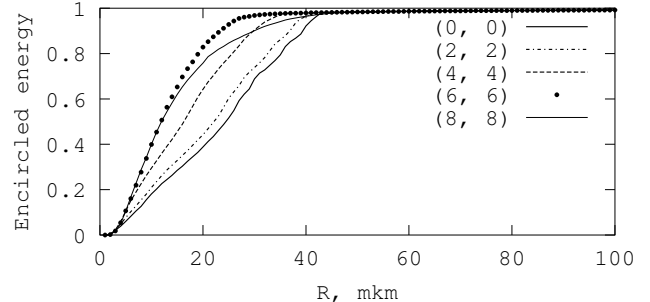
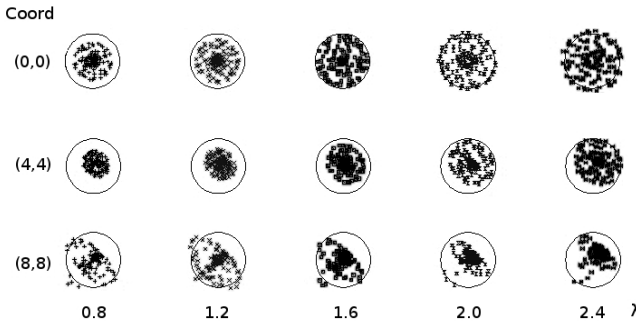


Figure 2: The computed spot diagrams of the focal reducer (left). The size of the circle on the diagram is  $1''$  ( $75\text{ }\mu\text{m}$ ). The field coordinates for the circle of confusion are given in the detector space (in mm). Wavelength is in  $\mu\text{m}$ . The right-hand panel shows the encircled energy (field coordinates are in mm).

of  $F = 100\text{ mm}$  and a  $2\omega = 16^\circ$  field of view. The collimator corrects the coma and astigmatism of the parabolic mirror of the 6-m BTA telescope ( $F = 24000\text{ mm}$ ,  $F/4$ ). The exit pupil relief and diameter are equal to 120 and 40 mm, respectively, and the back focal distance of the camera is equal to 10 mm.

The optical arrangement of the instrument allows it to operate in two modes: photometric and spectroscopic. The optical parts are made of  $\text{BaF}_2$ ,  $\text{CaF}_2$ ,  $\text{ZnSe}$ , and  $\text{SiO}_2$  (fused quartz, which is transparent in the IR) optical crystals. All surfaces are covered with anti-reflective coating optimized for the  $0.8 \div 2.5\text{ }\mu\text{m}$  wavelength interval.

Some of the chalcogenides used to make the optical parts of the instrument are rather fragile and therefore the corresponding lenses are mounted on individual protective holders, which, in turn, are mounted on the common holder of the collimator and camera.

According to our computations, the secondary spectrum of the focal reducer does not exceed  $\pm 150\text{ }\mu\text{m}$  in the  $0.8 \div 2.5\text{ }\mu\text{m}$  wavelength interval, and the chromatic aberration of position does not exceed 1 px (about  $20\text{ }\mu\text{m}$ ) at the edge of the field of view (see Fig. 2). Aberrations in the field do not exceed the size of two detector pixels (about  $40\text{ }\mu\text{m}$ ). The circle of confusion over the detector field ( $\pm 9.47\text{ mm}$ ,  $\pm 2/3$ ) for the operating wavelength interval fits within one arcsecond (about  $75\text{ }\mu\text{m}$ ).

To reduce the length of the instrument, diagonal mirrors are mounted in the parallel beam of the focal reducer. The main feature of the instrument that distinguishes it from its analogs is that it allows choosing the operating wavelength interval by adjusting the angle of incidence of the light beam onto the diffraction grating. To this end, the tilt angle of the diagonal mirrors is changed synchronously with the shift of the grating (via a sine drive mechanism).

The parameters of the lenses of the focal reducer are listed in Table I. The optics are designed to operate at a temperature of  $-40^\circ\text{C}$ . Simulations of the behavior of the focal reducer in the case of small deviations of the temperature from its design level showed the image

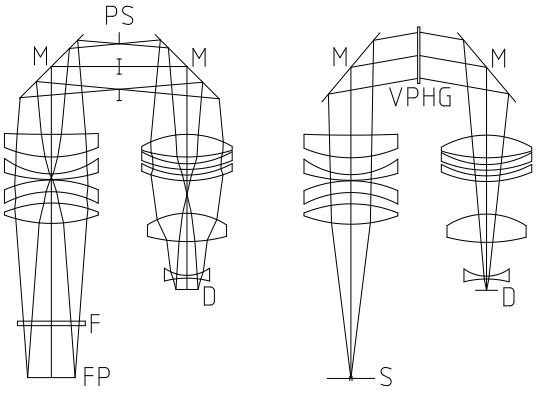


Figure 3: Diagram of the IR reducer operating in the photometric (left) and spectroscopic (right) modes. Here M are the diagonal mirrors; FP is the focal plane of the telescope; F is the filter; PS is the exit pupil stop; D is the detector; S is the slit, and VPHG is the diffraction grating.

properties to be sufficiently stable in the  $-40^\circ \pm 5^\circ\text{C}$  interval: only the focus of the entire system changes (and this change can be compensated by shifting the detector).

## 2.1. Photometric Mode

In this mode (see Fig. 3), the diagonal mirrors, M, are tilted at an angle of  $45^\circ$  to the light beam, and a cooled pupil stop, PS, is placed between them. For the 6-m BTA telescope the scale in the plane of the detector, D, is equal to  $0.255''/\text{px}$  and the field of view has the size of  $4.3'' \times 4.3''$ . The main interference filters (I, J, H, and K, and also filters for some molecular bands), F, are located in the divergent beam in front of the collimator. The image is focused by shifting the detector, D.

The exit pupil is cooled down to a temperature of about  $150\text{ K}$  in order to reduce thermal noise. Filter wheels (located in the divergent beam) and slit wheels (located in the focal plane of the instrument) are kept at the temperature of the cryostat “base” with no spe-

No.	$R_1$ , mm	$R_2$ , mm	$H$ , mm	$X$ , mm	$D$ , mm	$K, 10^{-6} K^{-1}$	Material/comments
FP	—	—	—	136.46	32	—	focal plane
1	119.88	-110.84	18.00	10.00	83	18.9	CaF <sub>2</sub>
2	-89.22	-103.61	10.34	0.50	83	7.1	ZnSe
3	143.21	69.60	5.00	14.93	83	0.5	SiO <sub>2</sub>
4	106.10	1104.77	20.00	120.00	83	18.4	BaF <sub>2</sub>
PS	—	—	—	120.00	40	—	exit pupil
5	80.23	-137.16	20.00	6.00	80	18.4	BaF <sub>2</sub>
6	-80.37	-105.66	5.00	5.00	80	0.5	SiO <sub>2</sub>
7	-83.63	-99.53	5.00	28.83	80	7.1	ZnSe
8	64.73	-135.61	25.00	29.92	70	18.4	BaF <sub>2</sub>
9	-34.30	80.14	2.50	10.00	40	0.5	SiO <sub>2</sub>
D	—	—	—	—	19	—	detector

Table I: Parameters of the focal reducer. No. – designation of a surface or the number of a lens;  $R_1$  and  $R_2$  – the curvature radii of the lens surfaces;  $H$  – the lens thickness;  $X$  – the distance between the neighboring surfaces;  $D$  – the lens aperture, and  $K$  – the thermal expansion coefficient. All quantities are given for the temperature of  $-40^{\circ}\text{C}$ .

Filter	I	J	H	K
Central filter wavelength $\lambda_0, \mu\text{m}$	0.88	1.25	1.62	2.20
Passband $\lambda_{FWHM}, \mu\text{m}$	0.22	0.30	0.20	0.60
Spectral flux density from Vega, $10^3 \text{Jy}$	2.55	1.57	1.02	0.64
Spectral flux density from Vega, $10^9 \text{photons}/(\text{m}^2 \cdot \text{s} \cdot \mu\text{m})$	43.73	18.96	9.50	4.39
Sky brightness, $m$	20.00	16.60	14.40	12.00
Sky brightness (continuum), $10^{-3} \text{Jy}/\text{arcsec}^2$	0.05	1.50	3.00	15.00
Sky brightness (continuum), $10^3 \text{photons}/(\text{m}^2 \cdot \text{s} \cdot \text{arcsec}^2 \cdot \mu\text{m})$	0.86	18.11	27.95	102.90

Table II: IR fluxes of a  $0^m$ -magnitude A0 V-type star in the Earth's atmospheric transparency windows; night-sky brightness according to [10]

cial cooling applied. Diagonal mirrors are coated with quartz-protected silver with a reflection coefficient of no less than 98% in the  $0.8 \div 2.5 \mu\text{m}$  wavelength interval.

To compute the limiting magnitude of the instrument in various parts of the spectrum, one must know the transmission of the “instrument-telescope” system, the spectral energy distribution of the object with atmospheric extinction taken into account, the angular size of the turbulent disk of the star, and the parameters of the detector.

We set the transmission of the instrument-telescope system equal to 0.5.

Table II lists the extra-atmospheric energy distribution in the spectrum of Vega, a  $0^m$ -magnitude A0 V-type star, for different photometric bands.

The flux in the spectral band is  $\Phi = \Phi_\lambda \Delta\lambda$ , where  $\Phi_\lambda$  and  $\Delta\lambda$  are the spectral flux density and passband, respectively. We multiply the flux by the effective area of the mirror  $S = 26 \text{ m}^2$  to obtain the radiation power of the star in the given spectral range. We then divide the power by the average photon energy (which we assume to be equal to the energy  $h\nu$  of a photon of the central wavelength of the filter passband) and multiply it by the transmission  $\eta_p$  of the optical path to obtain the number

of photons hitting the detector:

$$N_\gamma = \frac{\Phi S}{h\nu} \eta_p.$$

The image of an object of angular size  $\alpha = 1''$  in the primary focus of the 6-m BTA telescope has the linear size of  $L = F \cdot \alpha = 116 \mu\text{m}$ , where  $F$  is the focal distance of the telescope. If the optical parts of the instrument do not affect the aperture ratio of the beam arriving at the detector, such an object would illuminate 31 pixels of the HAWAII-I array (with a pixel area  $S_{pix} = x^2 = 18.5 \times 18.5 \mu\text{m}^2$ ). A factor of  $K$  reduction of the focal ratio decreases the image size by the same factor ( $116/K \mu\text{m}/\text{arcsec}$ ), and its area in pixels by a factor of  $K^2$ . For  $K = 1.6$  one arcsecond in the sky corresponds to 3.9 pixels on the detector. We take the average quantum efficiency of the HAWAII-I array equal to  $Q = 0.5$ . The number of electrons accumulated in one second by a single pixel of the detector is evidently equal to:

$$N_e = \frac{Q \cdot N_\gamma K^2 S_{pix}}{\pi (L/2)^2} = \frac{4K^2 Q S_{pix} N_\gamma}{\pi F^2 \alpha^2}.$$

The sky background further reduces the signal-to-noise ratio. Let  $s$  be the sky brightness (in photons/ $\text{m}^2/\text{sr}/\text{s}$ )

Band	I	J	H	K
Pixel size, arcsec			0.254	
Number of photons per second from Vega, $N_{\gamma 0}$ , $10^9$	125.08	73.93	24.71	34.25
Number of electrons per pixel per second from Vega, $N_e$ , $10^9$	5.15	3.05	1.02	1.41
Number of electrons per pixel per second from the sky, $N_{sky}$ , $10^3$	0.05	0.70	1.77	22.36
Detector noise during exposure $T_{exp} = 100$ s, $e^-$			20.0	
Estimated limiting magnitude (S/N= 5), $m$	22.85	20.90	19.21	18.19
Exposure for $N_\star - N_b = 1000$ , s	268.57	74.99	47.27	13.35
Limiting magnitude ( $T_{exp} = 100$ s and $N_\star - N_b = 1000$ ), $m$	21.78	21.21	20.02	20.37

Table III: Estimate of the limiting magnitude of the instrument when operating in the photometric mode

and  $N_{CCD}$ , the total detector noise (in electrons/s). The star light collected by the telescope (proportional to  $\Phi S$ ) produces  $N_\star$  electrons per second in the quantum well of a single pixel. Sky background radiation produces  $N_{sky}$  electrons in the same way (the sky flux is  $\Phi_{sky} = s\beta^2$ , where  $\beta$  is the angular size of the given sky area). To these we should add thermal electrons,  $D$ . As a result, we obtain:  $N = N_\star + N_{sky} + N_{CCD}$ .

In the case of Poisson statistics the signal-to-noise ratio of the system is  $B = N_\star/\sqrt{N}$ , from which we determine the minimum flux from the star detectable at a given S/N:

$$N_\star^2 - B^2 N - B^2(N_{sky} + N_{CCD}) = 0.$$

It follows from this that

$$N_\star = \frac{B^2}{2} \left( 1 + \sqrt{1 + \frac{4(N_{sky} + N_{CCD})}{B^2}} \right).$$

We can estimate  $N_{sky}$  in the given photometric band by the formula

$$N_{sky} = N_0 \cdot 10^{-0.4m_{sky}},$$

where  $m_{sky}$  is the surface brightness of the sky (in magnitudes per squared arcsecond) and  $N_0$  is the number of photoelectrons per pixel from an extended source with a surface brightness of  $0^m/\text{arcsec}^2$ .

According to the manufacturer's data, the array has a dark current of less than  $0.1 e^-/\text{s}$  and a readout noise of less than  $10 e^-$  (readout noise depends on the number of intermediate nondestructive signal readouts during exposure). We then estimate the limiting magnitude of the instrument for photometric observations by the formula  $\Delta m = -2.5 \lg(N_\star/N_0)$  (see Table III).

## 2.2. Spectroscopic Mode

In this mode the cooled pupil stop is replaced by a VPHG (see Fig. 3) in such a way that the turnable mirrors produce incidence angles on the grating that satisfy the Bragg condition for the given central wavelength. In this case, a set of slits is placed in the focal plane. Figure 4 shows how the spectral interval is selected by varying the Bragg angle by rotating the diagonal mirrors.

We now use equations from [9, 11] to estimate the parameters of the volume phase holographic grating (VPHG).

The diffraction efficiency of the VPHG in the planes parallel (the  $P$ -plane) and perpendicular (the  $S$ -plane) to the direction of the periodic structure of the grating can be estimated by the following formulas:

$$\eta_s = \sin^2 \left( \frac{\pi \Delta n_g d}{\lambda \cos \alpha_g} \right), \quad \eta_p = \sin^2 \left( \frac{\pi \Delta n_g d}{\lambda \cos \alpha_g} \cos(\alpha_g + \beta_g) \right),$$

where  $d$  is the thickness of the grating;  $\Delta n_g$  is the modulation amplitude of the grating refractive index  $n_g$  (often  $n_g(z) = n_g + \Delta n_g \cos[f(z)]$ );  $\alpha_g$  is the light incidence angle onto the grating plane of uniform  $n_g$  (inside the grating the angle is counted from the plane of discontinuity), and  $\beta_g$  is the diffraction angle (inside the grating). If  $\alpha_g = \beta_g$  and the Bragg condition

$$m \nu_g \lambda = 2n_g \sin \alpha_g,$$

where  $\nu_g$  is the modulation frequency of the grating refractive index, is satisfied, we obtain for the simplest case, when the lines are perpendicular to the grating plane and  $\alpha_g = \beta_g$ :

$$n_g \sin \alpha_g = n_{air} \sin \alpha, \quad \eta_s = \sin^2 \left( \frac{\pi n_g \Delta n_g d}{\lambda \sqrt{n_g^2 - \sin^2 \alpha}} \right),$$

$$\eta_p = \sin^2 \left( \frac{\pi n_g \Delta n_g d}{\lambda \sqrt{n_g^2 - \sin^2 \alpha}} \left( 1 - \frac{2 \sin^2 \alpha}{n_g^2} \right) \right).$$

The wavelength of maximum diffraction efficiency for the  $\beta_g = \alpha_g$  case can be estimated by the following formula:

$$\lambda_{max} = \frac{2n_g \Delta n_g d}{(1 + 2n) \sqrt{n_g^2 - \sin^2 \alpha}}, \quad n = \overline{1, \infty}.$$

We now compute the dispersion curve of the grating by the formula  $\alpha = \arcsin(m \nu_g \lambda / 2)$ , where  $m$  is the diffraction order. We thus derive the following formula for the reciprocal linear dispersion:

$$\frac{d\lambda}{dx} = \frac{2\Lambda \cos \alpha}{F_c} \left[ 1 - \left( \frac{\lambda}{2\Lambda} \right)^2 \right],$$

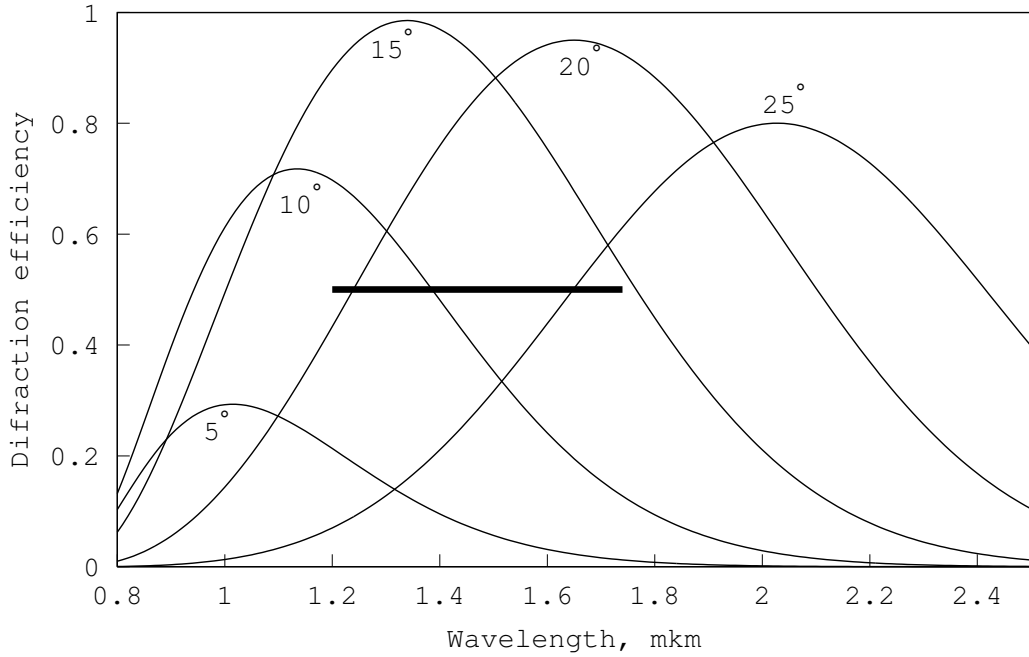


Figure 4: Diffraction efficiency as a function of wavelength. The bold line indicates the frame size.

Band	I	J	H	K
Number of electrons per pixel per second $N_e$ , $10^6$	6.15	2.67	1.34	0.62
Continuum				
Number of electrons per pixel per second from the sky, $N_{sky}$	0.05	1.05	1.62	5.95
Detector noise during exposure ( $T_{exp} = 1000$ s), $e^-$			110.0	
Estimated limiting magnitude, $m$ (S/N= 5)	19.76	17.91	16.96	15.47
Exposure for $N_s - N_b = 1000$ , $10^3$ ss	13.01	5.46	4.53	2.49
Limiting magnitude ( $T_{exp} = 1000$ s and $N_s - N_b = 1000$ ), m	16.97	16.06	15.32	14.48
OH lines				
Number of electrons per pixel per second from the sky, $N_{sky}$	0.08	1.48	8.43	66.48
Estimated limiting magnitude (S/N= 5), m	19.68	17.75	16.12	14.19
Exposure for $N_s - N_b = 1000$ , $10^3$ s	12.09	4.71	2.11	0.77

Table IV: Estimate of the limiting magnitude of the instrument when operating in the spectroscopic mode

where  $F_c$  is the focal distance of the focal reducer camera.

The angular width of the spectrum is  $\Delta\alpha = \alpha_{red} - \alpha_{blue}$ , where  $\alpha_{blue}$  and  $\alpha_{red}$  are the blue and red boundaries of the spectrum, respectively. The linear width of the spectrum is determined by the focal distance of the camera:  $l = F_c(\tan \alpha_{red} - \tan \alpha_{blue})$ . To efficiently use the detector surface, we must choose the focal distance of the camera based on the optimum relationship between the spectral resolution of the instrument (i.e., an element of the spectrum should occupy at least two to three pixels) and the halfwidth of the diffraction efficiency of the grating.

To make a spectrograph with a resolution of  $R \sim 3000$  at  $\lambda \sim 1.65 \mu m$ , the average size of the resolution element should be  $\delta\lambda = 1.65/3000 = 0.55 \text{ nm}$ . For the first order of diffraction the average angular width of the element of

resolution is  $\delta\alpha = \nu_g \delta\lambda$ . For example, for a 600 lines/mm grating ( $\nu_g = 6 \cdot 10^5 \text{ m}^{-1}$ ), this parameter is equal to  $\delta\alpha = 3.3 \cdot 10^{-4} \text{ rad} = 68''$ . “Placing” one element of resolution in two detector pixels,  $N_W = 2$  ( $w = 37 \mu m$ ), we estimate the focal distance of the camera:  $F = 11.2 \text{ mm}$ . In the case of a factor of  $K = 1.6$  focal ratio reduction the angular width of the slit is  $wK/F_{tel} = 0.51''$ .

To estimate the limiting magnitude of the spectrograph, we compute the average flux in atmospheric windows per spectrograph resolution element (by multiplying the flux density by the width of the resolution element).

For the 6-m BTA telescope the height of the spectrum of a star with a turbulent disk of angular diameter  $1''$  is  $N_H = 116/18.5/1.6 = 3.9 \text{ px}$ . A  $0.5''$  wide slit blocks 40% of the star’s image area, i.e., the flux per spectral resolu-

tion element should be multiplied by a factor of about 0.6 (if we ignore the Gaussian distribution of brightness over the turbulent disk of the star). The fraction of the area of a stellar image of diameter  $D$  that passes through a slit of width  $h$  can be determined by the formula

$$\eta_{slit} = 1 - \frac{2}{\pi} \left( \arccos \frac{h}{D} - \frac{h}{D} \sqrt{1 - \frac{h^2}{D^2}} \right);$$

Thus the power per one spectral resolution element outside the instrument is spread over  $N_{pix} \sim 8$  px. Given the transmission of the optics ( $\eta_P \approx 0.5$ ), the average diffraction efficiency of the grating ( $\eta_G \approx 0.5$ ), and the cutoff of a part of the image of the turbulent disk of the star at the slit ( $\eta_S \approx 0.6$ ), we compute the average number of photoelectrons per detector pixel per second as:

$$N_e = \frac{\Phi_\lambda \delta \lambda \cdot \lambda}{hc} \cdot \frac{SQ\eta_P\eta_G\eta_{slit}}{N_{pix}},$$

where  $\Phi_\lambda$  and  $\lambda$  are the spectral flux density of the star's radiation and the mid-wavelength of the spectral interval considered, respectively.

We can estimate in the same way the limiting magnitude for spectroscopy in the case of a 1000 s long exposure. We estimate the number of photoelectrons created as a result of the continuum sky brightness by the formula

$$N_{e, cont} = \frac{c}{\lambda^2} \frac{\Phi_{\lambda, sky} \lambda}{hc} \frac{\delta \lambda S \eta_P \eta_G Q \rho}{N_W} = \frac{\Phi_{\lambda, sky}}{h \lambda} \frac{\delta \lambda S \eta_P \eta_G Q \rho}{N_W},$$

where  $\rho$  is the pixel area in sky steradians. The corresponding estimates are listed in Table IV.

### 3. DESIGN OF THE INSTRUMENT

#### 3.1. Cryostat

The entire instrument is housed in a cylindrical cryostat (see Fig. 5) with the diameter and length of no greater than 550 and 650 mm, respectively. A part of the cryostat is occupied by the no-spill liquid-nitrogen container, made for the use in the primary focus of the 6-m BTA telescope. The cryostat was designed in accordance with the underlying principles of the cryostats made earlier for the 6-m BTA telescope [12]. Only two parts of the optical scheme require deep cooling: the detector and the exit pupil unit with diffraction gratings. Highly stable temperature is needed only for the detector.

Let us refer to the cryostat part that houses the flange with the optical window as the bottom part. The vacuum chamber consists of two asymmetrically arranged cylindrical containers: the lower container is located in the bottom, detachable part of the cryostat, and the upper container is located inside the liquid-nitrogen container

and has the form of a cylindrical depression in the container.

The flanges of the top and bottom parts of the cryostat facilitate its assembling and disassembling: by opening the top cap with the liquid-nitrogen container we get access to the entire internal arrangement of the cryostat.

The case of the vacuum chamber is made of titanium sheet. To reinforce the external walls of the cryostat and enhance their bearing capacity, rib stiffeners aligned along the vertical axis are welded to the external walls of both parts of the cryostat.

The shell ring of the lower chamber houses SNTs-type electric pressure seal connectors for the input/output of control signals and supply of power to the internal elements; windows facilitating assembly and disassembly of the entire structure, and the exhaust tube equipped with a safety valve.

A shutter is placed in front of the "warm" entrance window of the cryostat at the front flange. All optical and electromechanical equipment is located on a stainless steel welded frame mounted on the lower flange of the instrument via heat-insulating pads (see Fig. 6).

The cooled wheel with slits is located in the focal plane of the telescope. Behind this wheel two filter wheels are located in the divergent beam. These are followed, along the optical axis, by the collimator that forms the exit pupil of the instrument. Behind the collimator, two diagonal mirrors that turn the light beam by 180° are located. A diffraction grating is placed between the diagonal mirrors in the spectroscopic mode, and a cooled pupil stop — in the photometric mode. The objective followed by the detector are located behind the diagonal mirrors.

The liquid-nitrogen container is located in the top part of the cryostat and has the form of a cylinder with asymmetric depression. The shell ring and the top caps of the liquid-nitrogen container are made of stainless steel. The bottom ring of the container with heat-removing contact areas is made of copper.

The liquid-nitrogen container is fixed inside the cryostat case by welding it to the inner filler tube (which, in turn, is welded to the external nitrogen tube, which is welded to the external flange of the cryostat). In addition, the bottom part of the shell ring of the liquid-nitrogen container is stretched with kevlar threads to ensure the required stiffness of the structure.

The principal elements of the optical scheme are cooled by flexible copper cooling pipes mounted to the copper rim of the liquid-nitrogen container. To ensure the operation of the cryostat at any tilt angle, the caps of the container are connected inside it with copper cooling pipes.

The slit wheel has eight slots. Seven of these slots are occupied by slits and the eighth slot is left unoccupied to facilitate the photometric mode of operation. Both filter wheels have six slots with five slots occupied by filters and the sixth left free. The wheels are located on a common axis rigidly mounted on the main plate of the supporting frame. Each wheel is mounted on a pair of abutted bearings. The stepper motors that rotate the

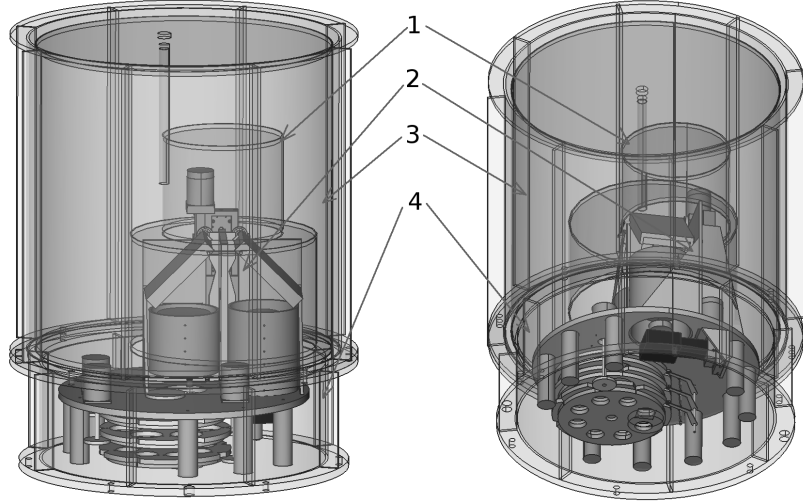


Figure 5: General view of the cryostat of the IR spectrometer: 1 – liquid nitrogen container; 2 – main frame; 3 – the top part of the cryostat cabinet, and 4 – the bottom part of the cryostat cabinet

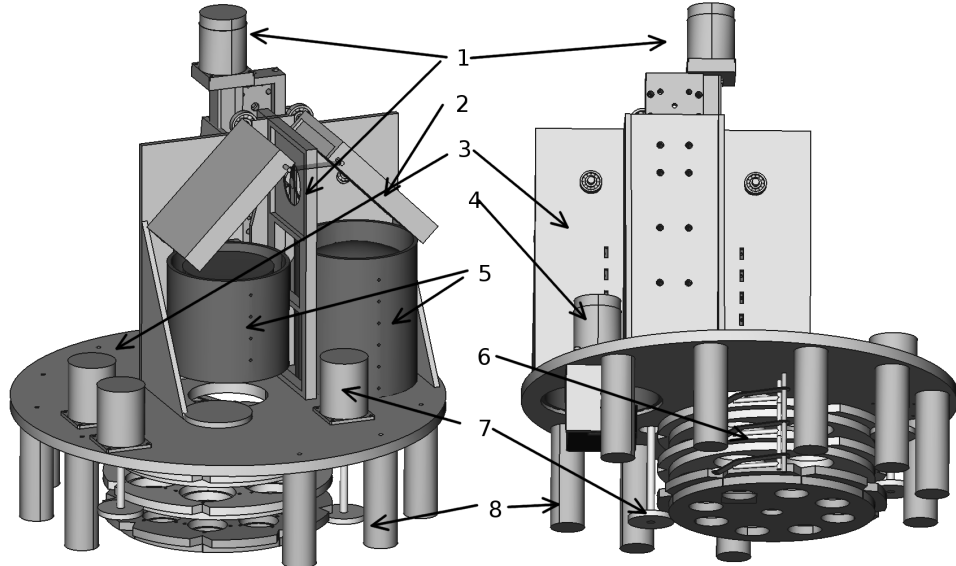


Figure 6: General view of the cryostated IR spectrometer: 1 – linear stage with the slit and pupil stop unit; 2 – diagonal mirrors; 3 – mounting frame of the instrument; 4 – focus stage; 5 – collimator and camera; 6 – wheel unit; 7 – wheel drives, and 8 – heat-insulating supports

wheels are fixed on the same plate. Torque is transferred via gears mounted on engine shafts; the other end of each gear shaft is left loose.

To reduce the cost and mass of the drive of diagonal mirrors and to simplify the synchronization of mirror rotation with the translational motion of the shifter with the grating unit and pupil stop, the translational motion of the shifter is transformed into rotational motion of mirrors via a sine drive mechanism. The mirrors are held by shaft axles fixed by a pair of abutted bearings.

The mechanics of the instrument are driven by standard devices: the linear stage 8MT173V-10 (Standa) is used for focussing (moving the detector); the linear stage 8MT175V-150 (Standa) moves the set of elements in the exit pupil and ensures the operation of the sine-drive mechanism; the stepper motors VSS42 drive the wheels.

The estimated mass of the instrument when assembled and nitrogen-filled is about 110 kg.

### 3.2. Sine-Drive Mechanism

The sine-drive mechanism consists of gimbal-mounted mirrors and a symmetric cam rigidly fixed onto the linear translator of the pupil stop and diffraction gratings. To reduce friction, the mirrors and the cam are coupled via bearings.

We modelled the sine-drive mechanism to determine the optimum positions for the mirror rotation axis, the axis of the thrust bearings, and the shape of the cam, and thereby minimize the offset of the exit pupil relative to the central plane of the shifter resulting from a change of the mirror tilt angle, and minimize the offset of the beam center relative to the center of the corresponding optical element on the shifter.

Figures 7 and 8 show the notation used in the model. Let us assume that the coordinates of the mirror rotation axis (point  $O'$ ) relative to the mirror center are  $(x', y')$ , and those of the axis of the thrust bearing (point  $O''$ ) are  $(x'', y'')$ . We denote the radius of the bearing by  $R$ . We count the mirror tilt angle,  $\alpha$ , from the horizontal direction and denote the cam apex angle by  $\gamma$ .

As a result of the vertical displacement of the cam by  $dZ_s$  the mirror tilt angle changes and the center of the reflected light beam shifts by  $dZ_r$ . The coordinates of point  $O''$  relative to point  $O'$  can be determined from Fig. 7:

$$\begin{cases} x_{O''} = (x'' - x') \cos \alpha - (y'' - y') \sin \alpha; \\ y_{O''} = (x'' - x') \sin \alpha + (y'' - y') \cos \alpha. \end{cases} \quad (1)$$

Point  $M$  where the bearing touches the cam lies on the normal to the cam that passes through point  $O''$ . As the cam moves, this point moves over its surface so that vector  $O''M$  undergoes parallel displacement. The coordinates of point  $M$  relative to point  $O'$  are:

$$\begin{cases} x_M = x_{O''} + R \cos \gamma; \\ y_M = y_{O''} - R \sin \gamma. \end{cases} \quad (2)$$

By tilting the mirror from  $0^\circ$  to angle  $\alpha$  we increase by  $\delta l = -x' \tan \alpha$  the length of the central ray incident on the mirror. In the case of  $\alpha = 0^\circ$ , the  $Y$  coordinate relative to the mirror plane of the point of incidence of the reflected ray on the diffraction grating is equal to  $y_{\text{ray}} = \delta l - w \cot 2\alpha$ .

The vertical offset of the cam, up to a constant term uniquely determined by the configuration of the system, is related to the coordinates of the point where the thrust bearing touches the cam:

$$Y_0 = \mathbf{C} + y_m + (w - x' - x_M) \cot \gamma, \quad (3)$$

Thus equations (1), (2) and (3) allow deriving the dependence of the cam shift on the incidence angle on the mirror. Inversion of this dependence yields the analytical relation between the cam shift and the incidence angle on the grating.

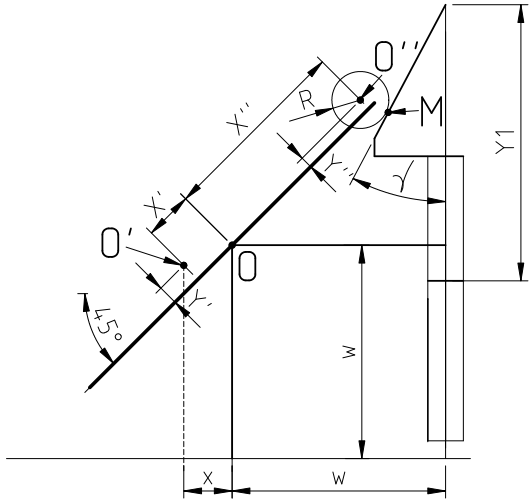


Figure 7: Sine-drive mechanism notation

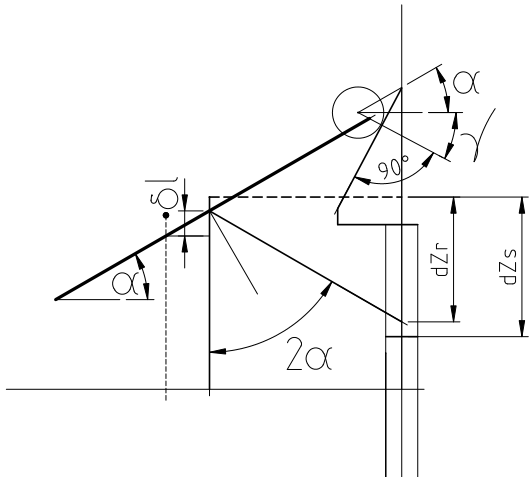


Figure 8: Principle of operation of the sine-drive mechanism

### 3.3. Frame for Mounting the Elements of the Instrument

All the optical and electromechanical equipment is located on a monolithic stainless steel frame, which is fixed to the bottom flange through heat insulating (ceramic or woven-glass reinforced) joints. Figure 6 shows the appearance of the frame with the elements mounted onto it.

The frame is made by welding together its structural elements, tempering the weld seams in a furnace and subsequent polishing and boring on a coordinate boring machine. The frame design ensures the required stiffness while facilitating the assembly and disassembly of its elements.

Instrument units are fixed to the frame with screw joints. Electric wires are fixed by passing them through the perforation in the frame walls and/or with collars.

Cooling pipes are fixed to the frame with screw joints or braces through heat-insulating joints.

### 3.4. Wheels

The spectrometer scheme includes three wheels: two filter wheels and one slit wheel.

The wheels are made of stainless steel and are rotated by stepper motors. The current position of a wheel is controlled using binary coding of the slots with the Hall sensors.

The slit wheel has eight through holes with a diameter of 35 mm. The slit kit consists of round metal frames with foil containing the slit of appropriate width stretched over them. The frames are fixed to the wheel surface with clamping plates. The slits occupy seven slots of the wheel. The eighth slot is left free to facilitate the photometric mode of operation.

Filter wheels have six slots with a diameter of 50 mm. The filters are fixed with metal inserts and clamping plates.

The wheels are located on a common axis that is rigidly fixed to the main plate of the supporting frame. The stepper motors that rotate the wheels are also fixed onto the same frame. An additional plate fixes the other end of the wheel axis. Each wheel is set on a pair of abutted bearings. Torque is transferred via the gears mounted on engine shafts; the other end of each gear shaft is left loose.

### 3.5. Optical Elements

The collimator and camera are placed on the vertical plate of the frame. The external mountings of the collimator and camera have the form of cylindrical structures with a 107-mm diameter. The crystal lenses are fixed in the external mount with auxiliary protective mounts that prevent damage to optics as a result of tensions arising from temperature variations (see Fig. 9).

By their design, the protective self-aligning mounts balance the tensions arising as a result of thermal deformations of mounts and lens material and stabilize the position of the lens relative to the optical axis. When the mount and lens temperature changes, the difference of the lens and mount sizes is compensated by moving the lens and the spring loaded retaining ring along the optical axis of the instrument by sliding the lens along the flats of the mount and retaining ring. The motion of the retaining ring is made possible by cylindrical guides. Protective mounts allow the optics to operate with a temperature change rate of up to 15°C/hour (the recommended rate is 6°C/hour).

The external mounts of the optics are fixed to the frame with screws. To ensure unique correct fixing of the mounts, the frame has arched sockets. Flexible cooling pipes are fed to the external mounts to cool the optics

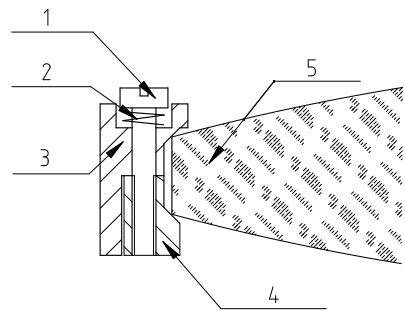


Figure 9: Protective mounts of crystal lenses: 1 – screw; 2 – spring; 3 – fixed part of the mount; 4 – moving part of the mount, 5 – lens

down to the operating temperature ( $-40^{\circ}\text{C}$ ).

### 3.6. Diagonal Mirrors

The instrument is equipped with two tilting mirrors to reduce the length of the optical system and allow changing the incidence angle of the light beam on the diffraction grating when operating in the spectroscopic mode. When the instrument is operated in the photometric mode, the mirrors are tilted by  $45^{\circ}$  relative to the light beam. When operating in the spectroscopic mode the mirrors change the tilt angle by  $30^{\circ}$  to  $45^{\circ}$  (in this case the sine-drive mechanism is used to synchronize the displacement of the diffraction grating and to transform the translational motion of the grating and pupil stop unit translator into mirror rotation).

The mirrors have the form of rectangular plates made of sital or another material whose reflective surface is coated with quartz-protected silver. The mirrors have overall dimensions of  $120 \times 80$  mm and a thickness of 15 mm. They are fixed in stainless-steel mounts with clamping plates and spring stops. Mirror mounts are placed on the vertical support of the spectrometer frame on shaft axles that are fixed by a couple of abutted bearings.

We modelled the sine-drive mechanism. The optimum choice of the position of the mirror rotation axis, the axis of the thrust bearing, the tilt angle, and the size of the pusher allows minimizing the offset of the exit pupil from the central plane of the stage resulting from a change of the mirror tilt angle. According to the model, the offset of the light beam from the center of the diffraction grating does not exceed 1.33 mm and the offset of the exit pupil center relative to the VPHG plane does not exceed 2.62 mm throughout the entire operating range of incidence angles. For the  $26^{\circ}$  cam apex angle of the sine drive mechanism the light incidence angle on the grating depends almost linearly on the vertical displacement of the translator.

### 3.7. Control and Recording Systems

The control system allows moving the elements of the instrument to change the mode of its operation, and provides the data on the position of these elements and their temperature. In the test mode the control system should be able to operate autonomously maintaining at least minimum functionality. In the normal mode of operation the control system is connected to the supervisory computer via USB, RS-232, or RS-485 interfaces. The system is powered either by a separate power-supply unit or by the power supply unit of the data acquisition unit.

Cryostat units do not require simultaneous operation of several drives and therefore the stepper motors are controlled commutatively: only one stepper motor can operate at a time. The engines are controlled via commercial stepper motor drivers.

The position of the elements is controlled by Hall sensors and end switches. The wheels reference positions are binary coded by the corresponding arrangement of magnets (the Hall sensors are placed on the stationary part) — this method reduces the number of sensors and thereby also the number of links and processed signals.

The registration system uses a cooled hybrid HgCdTe CMOS HAWAII multiplexer to perform numerical recording of the image produced by the optical system of the telescope and the spectroscopic/photometric equipment. The registration system is controlled by the same PC to which the control system is connected.

The registration system controls the operation modes of the detector, maintains stable operating temperature, controls exposure, readout, and saving of the images in FITS format.

### Acknowledgments

The team participating in the development and making of the IR spectrometer is rather big. We are grateful to all the members of this team:

- Specialists of the Advanced Design Laboratory of the Special Astrophysical Observatory (Nizhnii Arkhyz) directed by S. V. Markelov, who develop the registration system of the instrument;
- Specialists of Opto-Technological Service Co.Ltd. (St. Petersburg) directed by B. N. Ostrun, who make the optics of the collimator and the camera;
- Specialists of the Institute of Applied Physics of the Russian Academy of Sciences and the non- profit partnership “Experimental Design Bureau of High-Tech Development” (Nizhnii Novgorod) directed by V. F. Vdovin and Yu. Ya. Brodskii, who develop the preliminary design of the cryostat and mechanics of the instrument.

---

[1] S. E. Persson, R. Barkhouser, C. Birk et al. Society of Photo-Optical Instrumentation Engineers (SPIE) Conf. Ser. **7014**, 95 (2008).

[2] C. D. Mackay, R. G. McMahon, M. G. Beckett et al. Society of Photo-Optical Instrumentation Engineers (SPIE) Conf. Ser. **4008**, 1317 (2000).

[3] M. G. Beckett, C. D. Mackay, R. G. McMahon et al. Society of Photo-Optical Instrumentation Engineers (SPIE) Conf. Ser. **3354**, 431 (1998).

[4] M. G. Beckett, C. D. Mackay, R. G. McMahon et al. Society of Photo-Optical Instrumentation Engineers (SPIE) Conf. Ser. **2871**, 1152 (1997).

[5] K. Motohara, F. Iwamuro, T. Maihara et al. Publ. Astron. Soc. Japan. **54**, 315 (2002).

[6] S.-i. Okumura, E. Nishihara, E. Watanabe et al. Publ. Astron. Soc. Japan. **52**, 931 (2000).

[7] *Scientific Detectors for Astronomy 2005*, Ed by J. E. Beletic, J. W. Beletic, and P. Amico. (Springer, Berlin, 2006), p. 771.

[8] CIRSI measured properties: <http://www.ast.cam.ac.uk/~optics/cirsi/documents/properties.html>.

[9] S. C. Barden, J. A. Arns, W. S. Colburn, and J. B. Williams. Publ. Astron. Soc. Pacific. **112**, 809 (2000).

[10] C. R. Benn and S. L. Ellison. New Astronomy Reviews. **42**, 503 (1998).

[11] I. K. Baldry, J. Bland-Hawthorn, and J. G. Robertson. Publ. Astron. Soc. Pacific. **116**, 403 (2004).

[12] A. N. Borisenko, V. F. Vdovin, A. I. Eliseev, et al., Peterburgskii Zhurn. Elektron. **28** (3), 39 (2001).